Sustainable Energy & Fuels

ROYAL SOCIETY OF CHEMISTRY

PAPER

View Article Online
View Journal | View Issue

Cite this: *Sustainable Energy Fuels*, 2022, **6**, 502

Mesocrystal TiO_2 films: *in situ* topotactic transformation and application in dye-sensitised solar cells†

Bingyu Lei,[a] Arivazhagan Valluvar Oli,[b] Aruna Ivaturi [b] and Neil Robertson [*a]

Thin film ceramics and semiconductors play an important role in energy- and environment-related areas such as photovoltaics, energy storage and water purification. The morphology and structure of materials significantly affect their properties and performance in applications. Mesocrystal materials with a hierarchical structure and designable overall shape possess not only the properties from nanosized building-blocks but also collective functions from the crystallographically ordered assembly, meeting the criteria of high performance candidates in various applications. In this study, a facile and versatile method was developed to prepare mesocrystal films by simply making a printable paste of the topotactic precursor, followed by *in situ* topotactic transformation of printed films. Using TiO_2 as the model material, mesocrystal TiO_2 films made from NH_4TiOF_3 paste possess high surface area, crystallographic orientation of anatase nanoparticles and overall large particle size, performing well in dye-sensitised solar cells (DSSCs) as either single-layer photoanodes or additional scattering layers.

Received 11th November 2021
Accepted 16th December 2021

DOI: 10.1039/d1se01791h

rsc.li/sustainable-energy

Introduction

Thanks to its elemental abundance, nontoxicity, low cost, high chemical stability and unique physicochemical properties, titanium dioxide (TiO_2) has been intensively investigated in energy- and environment-related areas such as photocatalysis, hydrogen generation, Li-ion batteries, and solar cells.[1–5] To satisfy the criteria for different applications, there has been a lot of effort on tuning the size, crystallinity, shape and architecture of TiO_2 because these parameters can significantly affect its properties and performance. A very characteristic example is as photoanode for dye-sensitized solar cells (DSSCs).[6–9] A good photoanode requires specifically high dye loading capacity, efficient electron collection and transport and also a pronounced light-scattering ability. In most of the DSSCs studies, mesoporous anatase TiO_2 nanoparticle films made from commercially available TiO_2 paste (Ti-Nanoxide T/SP, Solaronix) are widely used. The highly dispersed nanoparticles (15–20 nm) possess a high surface area leading to efficient dye loading and high transparency ensuring favourable light penetration.[10,11] However, the negligible light scattering in nanoparticle films leads to a short pathway for incident light, limiting the photon absorption by the adsorbed dye molecules. To solve this problem, an additional scattering layer composed of large TiO_2 particles is generally applied on top of the transparent active layer in many reports to improve the light harvesting in DSSCs.[12] Another method is to develop hierarchical-structured TiO_2 as photoanode such as mesoporous TiO_2 microspheres,[13] TiO_2 nanoflowers[14] and hierarchical TiO_2 nanotube arrays.[15] It is also not surprising that the combination of the above two strategies, using TiO_2 with hierarchical structure as additional scattering layer has been shown to significantly enhance the light harvesting in DSSCs.[16,17]

As a recently-developed hierarchical structure, mesocrystals, consisting of nanocrystals with common crystallographic orientation, have drawn a lot of attention since they were first proposed by Cölfen in 2005 as the metastable intermediates in non-classical crystallization processes.[18] Over the past 16 years, mesocrystal structures were found or realized in a broad range of materials including biominerals and mimetics (*e.g.* sea urchin spines,[19] vaterite $CaCO_3$ (ref. 20)), metal oxides (*e.g.* ZnO,[21] TiO_2,[22] Fe_2O_3,[23] Co_3O_4 (ref. 24)), metal sulfide (*e.g.* ZnS[25]), *etc.*, and have been demonstrated to bring the material not only properties associated with individual nanoparticles but also collective properties and functions. TiO_2 mesocrystals ($mcTiO_2$) have been investigated in many applications and showed excellent performance, considering their advanced properties from the unique structure.[26–29] However, in most existing work, not only for $mcTiO_2$ but also for other mesocrystals, lengthy

[a]*School of Chemistry, The University of Edinburgh, David Brewster Road, Edinburgh EH9 3FJ, UK. E-mail: Neil.Robertson@ed.ac.uk*

[b]*Smart Materials Research and Device Technology (SMaRDT) Group, Department of Pure and Applied Chemistry, University of Strathclyde, Thomas Graham Building, Glasgow, G1 1XL, UK*

† Electronic supplementary information (ESI) available: Detail information of used dye and commercial pastes; XRD patterns of films from commercial pastes; SEM images of $mcTiO_2$ films from more heating rate; EDS spectrum and elemental composition of $mcTiO_2$; schematic illustrations of photoanodes; EIS parameters and plots as function of total electron concentration. See DOI: 10.1039/d1se01791h

hydrothermal or solvothermal treatments were always adopted to enable the 'bottom-up' nanocrystal oriented assembly.[26,27,30,31] To make mesocrystals, another 'top-down' strategy *via* topotactic conversion has also been explored in some cases.[32–34] This solid-to-solid transformation is based on crystallographic similarity between target product and the precursor, which is NH_4TiOF_3 in the case of anatase TiO_2.[22] Compared with a 'bottom-up' strategy, topotactic conversion uses a solid precursor as template, making it easier to design, control and predict the morphology and structure of the product. Considering the demands of TiO_2 films in many applications, such as photoanodes for solar cells, electrodes for energy storage and immobilised photocatalysts for easier reuse, a general and simple method to make functional mcTiO_2 films will broaden the application of mcTiO_2 in energy- and environment-related areas and bring the specific properties from the unique structure of mesocrystals to those applications.

In this work, we report a facile method to prepare functional mcTiO_2 films by making a printable paste of the NH_4TiOF_3 followed by *in situ* thermal topotactic transformation of printed NH_4TiOF_3 films, extending an approach that has received little prior attention.[35] The NH_4TiOF_3 precursor is prepared through an HF free route at room temperature and mixed with organic binders to form a viscous paste. The topotactic conversion occurs simultaneously with the thermal removal of organic components after film printing, significantly simplifying the manufacturing steps of mc$TiO_{2\ films}$. The obtained mcTiO_2 film was characterized by X-ray Diffraction (XRD), Scanning Electron Microscopy (SEM), Transmission Electron Microscopy (TEM), UV-Visible (UV-Vis) spectroscopy, Attenuated Total Reflection-Fourier Transmission Infrared (ATR-FTIR) analysis and tested in the example application of DSSCs to investigate the functions brought by the structural features. The mcTiO_2 films were applied as either single-layer photoanode or additional scattering layer for DSSCs using the commercial dye LEG4 as the photo-sensitizer. Compared with commercial transparent TiO_2 (Ti-Nanoxide T/SP, Solaronix), diffusing TiO_2 (Ti-Nanoxide D/SP, Solaronix) and reflective TiO_2 (Ti-Nanoxide R/SP, Solaronix), mcTiO_2 prepared from NH_4TiOF_3 paste possesses not only properties from individual nanoparticles but also collective functions, leading to satisfactory performance in DSSCs and promising prospects for other potential applications.

Experimental

Synthesis of NH_4TiOF_3

NH_4TiOF_3 powder was prepared from a room temperature hydrolysis reaction of $(NH_4)_2TiF_6$ with addition of ammonia solution, which is modified from a reported method.[28] Typically, 3.959 g $(NH_4)_2TiF_6$ (Acros Organics) was dissolved in 45 ml of H_2O, and then the solution was mixed with 5 ml 3 M ammonia solution under magnetic stirring. After stirring the solution for 5 min and letting it stand for 6 h at room temperature, the precipitate was collected by centrifugation and washed sequentially with water and ethanol, and dried in ambient conditions.

Preparation of NH_4TiOF_3 paste

The preparation of NH_4TiOF_3 paste follows a reported analogous method for TiO_2 paste with a few modifications.[36] Before making the paste, 1 g of two kinds of ethyl cellulose (EC) powders, *i.e.* EC (10 cP, Merck) and EC (30–70 cP, Merck) were dissolved in anhydrous ethanol respectively and stirred overnight at room temperature to get 10 g of EC stock solutions (10 wt%). They were labelled as EC-10 and EC-30 according to different viscosities. To prepare the paste, 0.278 g NH_4TiOF_3 was mixed with 0.65 g anhydrous terpineol solvent, 0.45 g EC-10 stock solution, 0.35 g EC-30 stock solution and 0.8 ml anhydrous ethanol. The amount of NH_4TiOF_3 was calculated to satisfy the Ti concentration as ~10.8 wt%, the same as commercial titania pastes from Solaronix. After stirring overnight, the mixture was sonicated for 2 min and stirred at 13 500 rpm for 1 min using an ultra-terrax mixer. The sonication and stirring procedure was repeated 3 times. Ethanol and water were then removed by rotary-evaporation at 40 °C.

Preparation of TiO_2 photoanodes

Fluorine-doped tin oxide (FTO)-coated glass substrates (TEC7, Merck) were cut into pieces of size 3 cm × 4 cm (for 4 cells), and sonicated in 2 vol% Hellmanex detergent solution for 30 min, DI water for 15 min and rinsed with ethanol. Then they were dried with hot air and treated by UV/ozone for 20 min. Prior to screen printing, FTO substrates were pre-treated by a 40 mM $TiCl_4$ aqueous solution at 70 °C for 30 min, followed by a water rinse and a heat treatment at 500 °C for 30 min. For the single layer DSSCs, the NH_4TiOF_3 paste or commercial paste (nanoparticle only paste Ti-Nanoxide T/SP, mixed titania particle paste Ti-Nanoxide D/SP, and large titania particle only paste Ti-Nanoxide R/SP) was screen-printed on top of $TiCl_4$ treated FTO substrates through a 90 polyester screen with 4 circles ($D = 6$ mm). The films were sintered at 500 °C for 2 hours using different temperature ramps. The obtained TiO_2 films were named as F (mesocrystal TiO_2 from NH_4TiOF_3 paste), T (transparent TiO_2 from Ti-Nanoxide T/SP), D (diffusing TiO_2 from Ti-Nanoxide D/SP), and R (reflective TiO_2 from Ti-Nanoxide R/SP). A numeric suffix will be used to note the heating rate. For example, F-2 means 1 layer of TiO_2 film made from NH_4TiOF_3 paste with a heating rate of 2 °C min^{-1}. For the two-layers cells, Ti-Nanoxide T/SP was used to print the transparent active TiO_2 layer and sintered at 500 °C for 15 min. Additional scattering layers were prepared by depositing screen-printed NH_4TiOF_3 paste or commercial paste (Ti-Nanoxide D/SP or Ti-Nanoxide R/SP) on top of the transparent TiO_2 layer, followed by sintering at 500 °C for 2 hours with a heating rate of 2 °C min^{-1}. The obtained films were named as TF, TD, and TR respectively.

Fabrication of dye-sensitized solar cell

The TiO_2 films were pre-heated at 120 °C for 30 minutes before being immersed in a dye bath containing 0.2 mM LEG4 (Dyenamo, Fig. S1†) in acetonitrile/*tert*-butanol (1 : 1, v/v). After sensitization for 20 hours, the electrodes were rinsed with acetonitrile and dried in air. Counter electrodes were prepared

by doctor-blading platinum precursor paste (Solaronix Platisol-T) on FTO substrates followed by heating in air at 450 °C for 15 min. The working electrode and counter electrode were assembled together into a sandwich type cell and sealed with a hot-melt Surlyn film. An I^-/I_3^- electrolyte solution was injected through a pre-drilled hole in the counter electrode by vacuum back filling and the hole was then sealed with Surlyn cover and a microscope coverslip. The electrolyte was composed of 0.1 M LiI, 0.05 M I_2, 0.6 M 1,2-dimethyl-3-propylimidazolium iodide (DMPII), 0.5 M 4-*tert*-butylpyridine (*t*BP) in acetonitrile. Fig. S2† shows digital photos of the example DSSC devices.

Characterization

XRD was carried out on a Bruker D2 PHASER using CuKα radiation. UV-Vis absorption/diffuse reflectance spectra (DRS) were obtained using a JASCO V-670 UV/Vis/NIR spectrophotometer. Infrared (IR) spectra from 4000 to 500 cm^{-1} were recorded on a PerkinElmer Spectrum 65 ATR-IR spectrometer. To prepare film samples for XRD, UV-Vis DRS and IR characterizations, NH_4TiOF_3 paste or commercial TiO_2 pastes were doctor-bladed on glass slide with the thickness controlled by 1 layer of Scotch tape, followed by a drying process at 120 °C for 10 min and a sintering process if needed. Surface and cross-sectional SEM images of samples were collected using a ZEISS SIGMA Field Emission SEM, operated in SE2 mode with a 10 kV accelerating voltage. To prepare specimens for cross-section analysis, the substrates were scored before screen-printing. The substrates were broken along the score after preparation of films and adhered on a stub with the cross section facing up. TEM, Selected-Area Electron Diffraction (SAED) and Electron Dispersive Spectroscopy (EDS) were carried out using a FEI Titan Themis microscope. Photocurrent density–voltage (*J–V*) curves were recorded on an Autolab potentiostat (Metrohm) with class AAA SLB300A solar simulator (Sciencetech) as the light source. The light intensity was calibrated to AM1.5G using a silicon reference cell. The active area of the solar cell was fixed with a black metal mask with a circular aperture of 0.0707 cm^2 (d = 3 mm). The frequency-modulated electrochemical impedance spectroscopy (EIS) was recorded with a similar setup to that of the *J–V* measurements. The frequency range was set to 1 MHz to 0.05 Hz with an AC voltage amplitude of 10 mV. The measurements were performed under white light emitting diode (LED) illumination with adjustable intensity. The plots were fitted using the ZView (Scribner Associates) software. Incident photon-to-current conversion efficiency (IPCE) was recorded with a photo-spectrometer setup (Bentham PVE300) by illuminating the solar cell with a modulated monochromatic light (xenon and quartz halogen lamps) through 1.85 mm slit. The incident light was calibrated with a reference silicon photodiode and the spectral resolution was set to 5 nm.

Results & discussion

NH_4TiOF_3 powder samples were synthesized based on a reported method, modified to have an increased reaction volume.[28] The XRD pattern in Fig. 1a matched well with the

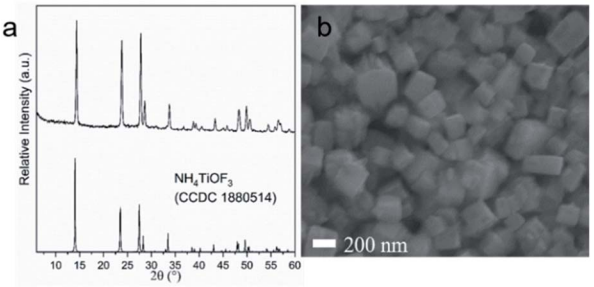

Fig. 1 (a) XRD pattern and (b) SEM image of NH_4TiOF_3.

powder diffraction pattern of reported NH_4TiOF_3 (CCDC 1880514) simulated using Mercury software,[37,38] indicating that phase-pure NH_4TiOF_3 was successfully obtained. Fig. 1b shows the SEM image of the NH_4TiOF_3 particles with a diameter range of 200–350 nm, in line with the size range for optimum visible light Mie scattering.[39]

NH_4TiOF_3 powders were mixed with organic binders to prepare printable pastes. Doctor-bladed films with thickness controlled by 1 layer of Scotch tape were sintered at 500 °C for 2 hours with different heating rate, namely 1 °C min^{-1}, 2 °C min^{-1}, 5 °C min^{-1} and 10 °C min^{-1}. Fig. S3† shows a digital photo of the doctor-bladed film on a piece of glass slide (1.8 cm × 2.6 cm). No cracking or flake-off was observed after the sintering procedure, indicating a good mechanical adhesion of the printed film. XRD patterns of the obtained films are shown in Fig. 2a, confirming that all samples were pure phase anatase (ICDD 86-1156). The crystallite domain size of each sample was calculated from the full width at half maxima (FWHM) of (101) diffraction peak (2-theta = 25.3°) using the Scherrer equation, and assuming negligible instrumental broadening (Table 1). In DSSCs, the crystallinity of TiO_2 is associated with the trap states distribution of the photoanode, which will have influence on the charge recombination rate thereby affecting the power conversion efficiency (PCE).[40] Sample F-2 under the heating rate of 2 °C min^{-1} shows the largest average crystal size among all the samples, which may lead to a relatively-lower charge

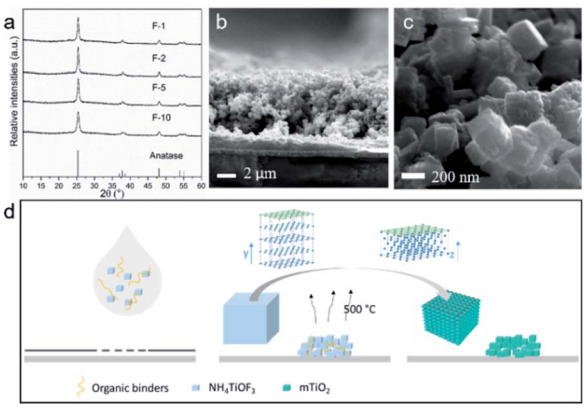

Fig. 2 (a) XRD patterns of $mcTiO_2$ films. (b) SEM and (c) TEM image of $mcTiO_2$ under heating rate of 2 °C min^{-1}. (d) Schematic illustration of the *in situ* topotactic transformation.

Table 1 Comparison of the crystal sizes, dye uptake capabilities and photovoltaic properties of single-layer TiO_2 photoanodes. All the samples were sintered at 500 °C for 2 hours with a heating rate indicated by the numeric suffix[a]

TiO_2 photoanode	Composition	D[101] (nm)	Dye loading (nmol cm^{-2})	V_{OC} (V)	J_{SC} (mA cm^{-2})	FF	PCE (%)
F-1	mcTiO_2 made from	17.93	56.28	0.69 (0.69 ± 0.01)	8.77 (8.35 ± 0.31)	0.70 (0.71 ± 0.02)	4.26 (4.09 ± 0.15)
F-2	NH_4TiOF_3 paste	19.63	52.21	0.73 (0.72 ± 0.00)	9.14 (9.10 ± 0.04)	0.72 (0.69 ± 0.02)	4.78 (4.57 ± 0.17)
F-5		17.56	60.25	0.72 (0.71 ± 0.01)	9.31 (9.19 ± 0.09)	0.68 (0.68 ± 0.00)	4.55 (4.49 ± 0.06)
F-10		13.65	53.02	0.68 (0.68 ± 0.01)	9.43 (8.62 ± 0.57)	0.70 (0.67 ± 0.03)	4.50 (3.90 ± 0.44)
T-2	Transparent TiO_2	17.80	59.89	0.72 (0.72 ± 0.01)	10.86 (10.66 ± 0.25)	0.66 (0.63 ± 0.02)	5.14 (4.81 ± 0.20)
D-2	Diffusing TiO_2	31.59	55.84	0.73 (0.73 ± 0.01)	10.21 (9.95 ± 0.29)	0.72 (0.70 ± 0.02)	5.35 (5.04 ± 0.32)
R-2	Reflective TiO_2	56.43	16.27	0.74 (0.73 ± 0.01)	3.49 (3.37 ± 0.19)	0.71 (0.71 ± 0.01)	1.84 (1.74 ± 0.10)

[a] Mean values ± s.d. are obtained from 3–4 devices for each TiO_2.

recombination rate and higher photovoltages when applied in DSSCs. However, larger crystallite size may also result in smaller surface area therefore a lower dye coverage and current density. The performance of TiO_2 in DSSCs requires an optimal balance between two parameters.

To better evaluate the properties and performance of mcTiO_2 made from NH_4TiOF_3 paste, three commercial available pastes were selected as references, namely nano-particle only paste Ti-Nanoxide T/SP, mixed titania particle paste Ti-Nanoxide D/SP, and large titania particle only paste Ti-Nanoxide R/SP. More details of commercial pastes and the comparison with NH_4TiOF_3 paste are listed in Table S1.† TiO_2 films from commercial available pastes were also made by doctor-blading and sintering at 500 °C for 2 hours with a heating rate of 2 °C min^{-1}. XRD patterns of obtained reference TiO_2 (T-2, D-2 and R-2) are given in Fig. S4.† The crystallite domain size for these samples were also calculated from (101) diffraction peak and collected in Table 1, which shows a consistent order with the particle sizes. Compared with the crystallite size of the reference TiO_2, mesocrystal F-2 sample is in the middle of the order, which may offer the possibility of a balanced crystallinity and surface area.

Also, the approximate 20 nm size of the crystallites has been generally regarded as optimal for the conventional I^-/I_3^- electrolyte-based DSSCs.[41]

SEM images of mesocrystal TiO_2 annealed under different heating rate are given in Fig. 2b, c and S5.† It is clear to see that after sintering at 500 °C, all samples retained the overall shapes and sizes of the original NH_4TiOF_3 powders, with 200–350 nm particle range which is beneficial for visible light scattering. The high-resolution images indicate that the cubic particles are built of smaller nanoparticles, consistent with the crystalline-domain size determined by the Scherrer equation. The most typical feature of a topotactic conversion is that the product keeps the overall shape and size of precursor but alters the crystal structure to a mesocrystal form, which means the building blocks of products from topotactic transformation should be crystallographically ordered.[22] This can be proven by TEM. Fig. 3 shows the TEM images of a TiO_2 sample sintered at 500 °C for 2 hours with a heating rate of 2 °C min^{-1}. The TEM image of a typical particle shows a rhombus shape and the porous structure (Fig. 3a). The corresponding SAED pattern of the circled area shows a typical mesocrystal diffraction pattern (single-crystal like with minor distortion), which can be indexed to the [11−1] zone of anatase.[42] From higher magnification in Fig. 3b, square facets of nanoparticles can be clearly recognised, corresponding to exposed {001} facets of truncated bipyramidal anatase (see inset of Fig. 3b). The size of nanoparticles is consistent with the crystalline domain size calculated from XRD results. The high resolution TEM image (Fig. 3c) shows planes with lattice spacing of 0.36 nm, corresponding to the (101) and (011) planes of the anatase phase, and the 82° angle between (101) and (011) matches the theoretical value calculated from the lattice constants of anatase (ICDD 86-1156). The EDS analysis (Fig. 3d–f) shows dominant Ti (44.4%) and O (54.5%) elements and homogeneous distribution. The negligible concentration of N (1.09%) and F (0.0147%) (see Fig. S6 and Table S2†) suggests the efficient removal of N and F after the sintering progress. Collectively, it can be confirmed that anatase TiO_2 mesocrystals were successfully obtained.

ATR-FTIR analysis was used to provide more information on the topotactic conversion process. Samples scratched from NH_4TiOF_3 doctor-bladed film which was only dried at 120 °C for 10 min and mcTiO_2 film after sintering at 500 °C for 2 hours were measured, together with powder form NH_4TiOF_3 and ethyl cellulose as references (Fig. 4). Before sintering at 500 °C, NH_4TiOF_3 sample (Fig. 4c) showed absorption peaks of both

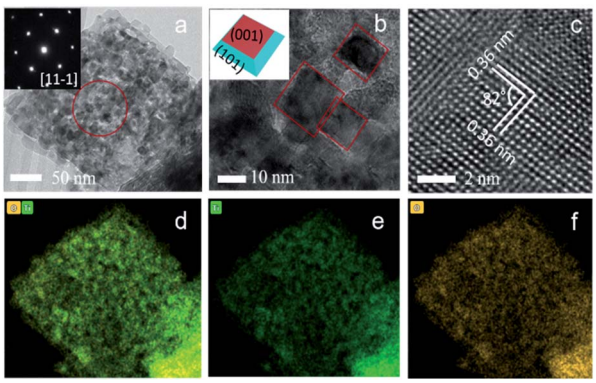

Fig. 3 (a–c) TEM images of mcTiO_2 with different magnifications. The inset of (a) shows the SAED pattern of the circled area. (d)–(f) TEM-EDS maps of mcTiO_2, showing the high-angle annular dark field image (HAADF) of oxygen (yellow), and titanium (green) maps of the area.

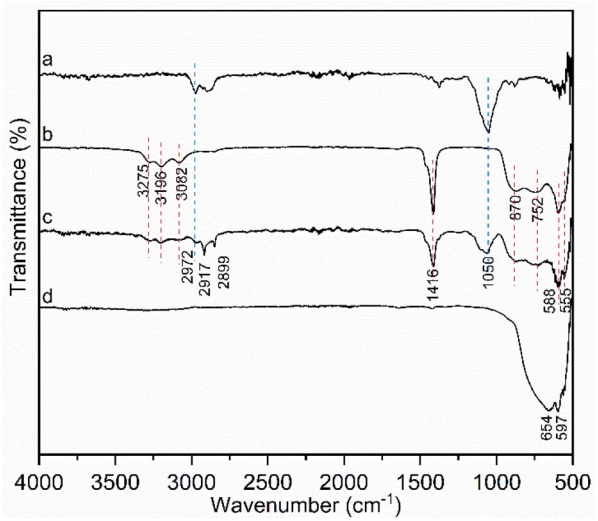

Fig. 4 ATR-FTIR spectrum of (a) ethyl cellulose, (b) powder form NH_4TiOF_3, (c) NH_4TiOF_3 scratched from doctor-bladed film and (d) $mcTiO_2$ scratched from doctor-bladed film after sintered at 500 °C for 2 hours.

NH_4TiOF_3 and organic binders. The bands at 3196 cm^{-1}, 3082 cm^{-1} and 1416 cm^{-1} are attributed to the ν_3, ν_1 (or $\nu_2 + \nu_4$) and ν_4 modes of NH_4^+ respectively.[32] The disappearance of all these peaks in $mcTiO_2$ sample (Fig. 4d) indicates the removal of ammonium after the topotactic conversion. Due to the hydroscopic nature of NH_4TiOF_3, deformation band of adsorbed water at 3275 cm^{-1} appeared in Fig. 4c, which was, however, not detected in the $mcTiO_2$ sample. Other typical absorption peaks of NH_4TiOF_3 were observed between 1000 cm^{-1} to 500 cm^{-1}. The band at 870 cm^{-1} is ascribed to ν (Ti=O) (terminal oxygen) or Ti–O–Ti antisymmetric stretching.[43] The band at 752 cm^{-1} corresponds to a combination of lattice mode of Ti–O and Ti–F bands, which is a typical feature of oxofluorotitanates.[44] The bands at 588 cm^{-1} and 555 cm^{-1} were due to Ti–F and Ti–O respectively.[32,44] After calcination, the product $mcTiO_2$ displayed only a broad stretching vibrational Ti–O–Ti absorption peak in this range, indicating the decomposition of Ti–F after topotactic conversion. The vibrations between 3000 cm^{-1} and 2840 cm^{-1} are associated with C–H stretching of either ethyl cellulose or terpineol added as organic binders,[45,46] which are not observed in $mcTiO_2$ sample, indicating the combustion of organic additives after the topotactic conversion. Another indicative absorption peak at 1050 cm^{-1}, which may be from –C–O–C– stretching of the pyranose ring in ethyl cellulose,[46] is also not found in the spectrum of $mcTiO_2$ sample. In short, the NH_4TiOF_3 film made from NH_4TiOF_3 paste undergoes a topotactic transformation to form mesocrystal TiO_2 and a simultaneous removal of organic binders. A schematic illustration of this *in situ* topotactic transformation process is given in Fig. 2e. More generally, this strategy could be transferrable to other functional ceramics as long as the thermal topotactic transformation can be applied.

To evaluate the photovoltaic performance of anatase $mcTiO_2$, the obtained anatase $mcTiO_2$ films were firstly tested as

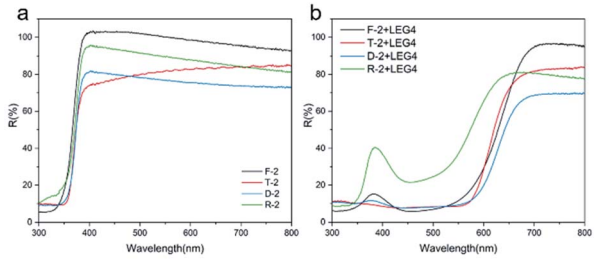

Fig. 5 UV-Vis DRS spectrum of TiO_2 films sintered from different paste at 500 °C for 2 hours with a heating rate of 2 °C min^{-1} (a) before dye sensitisation and (b) after sensitised by LEG4 dye.

single-layer photoanodes. Considering the low thickness of the single-layer TiO_2 obtained from screen-printing (4–6 μm, Fig. 2b), LEG4 dye with high extinction coefficient was selected as the sensitizer.[47] To investigate the light scattering effect and dye-loading capacity of single-layer $mcTiO_2$ films, doctor-bladed films were tested by UV-Vis DRS before and after LEG4 dye adsorption. According to the UV-Vis DRS spectrum in Fig. 5a, before absorbing dye molecules, bare anatase $mcTiO_2$ (sample F-2) has the highest reflectance compared with all samples from commercial pastes, indicating the highest light scattering ability. This is because of the optimal particle size of anatase $mcTiO_2$ inherited from the precursor NH_4TiOF_3 after the topotactic conversion. After dye loading (Fig. 5b), the reflectance in the visible range of all the samples drastically decreased due to the light absorption by dye molecules. The lower decrease from R-2 sample indicates a poor dye uptake capability. Quantified dye coverage on different TiO_2 films is collected in Table 1. It is shown that all $mcTiO_2$ films made from NH_4TiOF_3 paste possess comparable dye uptake capability to that from Solaronix T and Solaronix D and much higher dye loading than Solaronix R, confirming the high surface area arising from individual nanoparticles in $mcTiO_2$.

The single-layer DSSCs were characterized by measuring *J–V* behaviour under 1 sun illumination. The results are given in Fig. 6 and also summarized in Table 1. Fig. 6a shows the comparison among DSSCs with anatase $mcTiO_2$ as photoanodes with different temperature ramp during the $mcTiO_2$ film annealing process. In general, the performance of DSSCs under different conditions varies in a very small range in terms of all

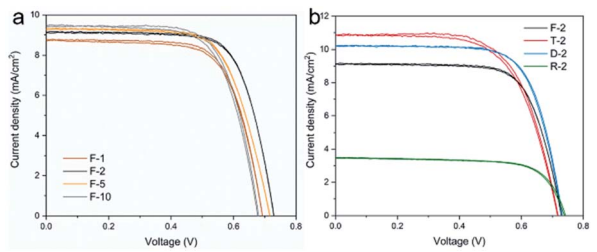

Fig. 6 *J–V* curves of single-layer DSSCs based on (a) $mcTiO_2$ photoanodes annealed under different heating rates (1, 2, 5 and 10 °C min^{-1}); and (b) different TiO_2 photoanodes (all annealed at a heating rate of 2 °C min^{-1}).

parameters. Among all the heating rate, the samples annealed with a ramp of 2 °C min^{-1} gave relatively higher PCE, resulting from the optimal balance between the open circuit voltage (V_{OC}) and the short circuit current density (J_{SC}), despite that samples annealed with a ramp of 5 °C min^{-1} possessed higher dye loading and correspondingly higher J_{SC}. Films made from commercial pastes were also tested in DSSC devices to compare with the performance of mcTiO$_2$ as single-layer photoanodes (Fig. 6b). Compared with Solaronix T and D, mcTiO$_2$-based DSSCs F-2 showed comparable V_{OC} and fill factor (FF) but a bit lower J_{SC}. As a result, the PCE of F-2 (4.57 ± 0.17%) was lower than T-2 and D-2 by 0.24% and 0.47% respectively. The slight drop in photocurrent is attributed to the big particle size. Even though mcTiO$_2$ can adsorb comparable amount of dye molecules to nanoparticle based films as discussed above, the excellent light scattering and reflection may lead to the waste of backward scattered light (see Fig. S7†), therefore reducing overall light harvesting. This is a drawback of mcTiO$_2$ when applied in single-layer photoanodes, but can be utilized as a benefit when it is applied as the additional scattering layer, which will be discussed in the next section. Solaronix R was also used as the reference TiO$_2$. The DSSCs based on large particle TiO$_2$ (R-2) showed the highest V_{OC} among all devices. However, this is with the sacrifice of J_{SC} due to the lowest dye loading, which is not favourable for single-layer photoanodes. The mcTiO$_2$ particles have similar overall particle size to R but higher porosity due to the mesocrystal structure. As a result, mcTiO$_2$ DSSCs F-2 offer similar V_{OC}, but much higher J_{SC} than devices based on R, resulting in a better performance as single-layer photoanodes.

To better understand the interfacial charge transfer mechanism of mcTiO$_2$ based single-layer DSSCs, EIS measurements were conducted under white LED illumination at open circuit conditions. By varying the light intensity, the V_{OC} can be tuned and hence the quasi-Fermi level in the photoanode. During all measurements, a 10 mV perturbation was applied in the 0.05 to 1 MHz frequency range. Fig. 7a and b display examples of Nyquist plots for DSSCs based on different single-layer photoanodes under a bias of 0.7 V. There are two semicircles in each plot. The first one in the high-frequency region denotes the electron transfer at the Pt/electrolyte interface, and the other semicircle represents the electron recombination at the TiO$_2$/dye/electrolyte interface. A transmission line equivalent circuit model[48] shown in the inset of Fig. 7b was used to extract electron transfer parameters of cells from all Nyquist plots under a series of applied bias potentials. Examples of fitted results from plots under 0.7 V are shown in Table S3.†

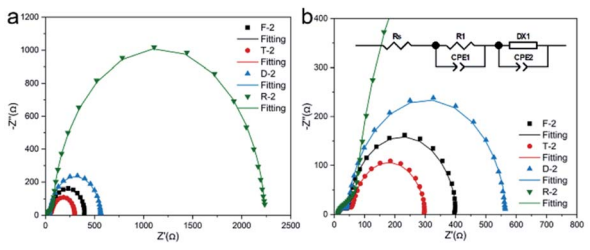

Fig. 7 (a) Nyquist plots for single-layer DSSCs measured at 0.7 V under white light LED illumination. (b) Magnified version of (a). Inset of (b) equivalent circuit for the electrochemical impedance fitting. R_s: series resistance; R_1: resistance at the Pt/electrolyte interface; CPE1: capacitance at the Pt/electrolyte interface, derived from a constant phase element; DX1: transmission line element for the porous electrode (type 11: Bisquert #2); CPE2: chemical capacitance at the triple contact FTO/TiO$_2$/electrolyte interface, derived from a constant phase element.

The chemical capacitance, C_μ, provides information on the electronic structure of TiO$_2$ in DSSCs as[49]

$$C_\mu = C_0 \exp\left(\frac{\alpha q V}{k_B T}\right) \quad (1)$$

$$C_0 = L(1-p)\alpha \frac{q^2 N_t}{k_B T} \exp\left[\frac{\alpha(E_{redox} - E_c)}{k_B T}\right] \quad (2)$$

with N_t the total number of trap states below the conduction band, L the film thickness, p the porosity of the film, q the elementary charge, k_B the Boltzmann constant and $(E_{redox} - E_c)$ the energy difference between redox potential of electrolyte and conduction band of TiO$_2$. Fig. 8a shows the typical exponential increase of C_μ with the increasing applied potential and according to eqn (1), the exponential trap distribution parameter α can be extracted from the slope. Different α values for cells with different single-layer photoanodes, as shown in Table S3,† reflect their different depth of trap distributions.[50] The highest α of cell F indicates the shallowest distribution of trap states and relatively smaller proportion of deep traps, which would be beneficial for charge collection *via* the trap–detrap process.[51,52] This could have benefited from the orientation of cubic nanoparticles in the mesocrystal structure, since many studies have demonstrated the strong dependence of the trap states distribution on the structural order of the charge carrier transport films.[53,54] In addition to the morphology, the crystallinity of TiO$_2$ also impacts the density of states (DOS) in terms of both bulk and surface trap concentrations,[55] which is denoted as N_t in eqn (2). According to Fig. 8a, the C_μ values of the cells follow the order of T > D ~ F > R, consistent with that expected from their order of crystallinity estimated from crystallite domain size, implying that the effect from crystallinity makes the main contribution to the DOS of photoanodes.

The recombination resistance (R_{rec}) at the TiO$_2$/dye/electrolyte interface was plotted *versus* applied potential in Fig. 8b. The order of the R_{rec} for all TiO$_2$ follows R > D ~ F > T, consistent with the order of their V_{OC} under 1 sun illumination. The potential dependence of R_{rec} follows the Buttler–Volmer relationship as[49]

$$R_{rec} = R_0 \exp\left[-\frac{\beta q V}{k_B T}\right] \quad (3)$$

$$R_0 = \frac{\sqrt{\pi \lambda k_B T}}{q^2 L \alpha k_r c_{ox} N_s} \exp\left[\frac{\alpha(E_c - E_{redox})}{k_B T} + \frac{\lambda}{4 k_B T}\right] \quad (4)$$

where λ is the reorganization energy of acceptor species, and β is the transfer coefficient, k_r the rate constant accounting for recombination kinetics, N_s the total number of surface states contributing to the recombination. By use of eqn (3), the β for

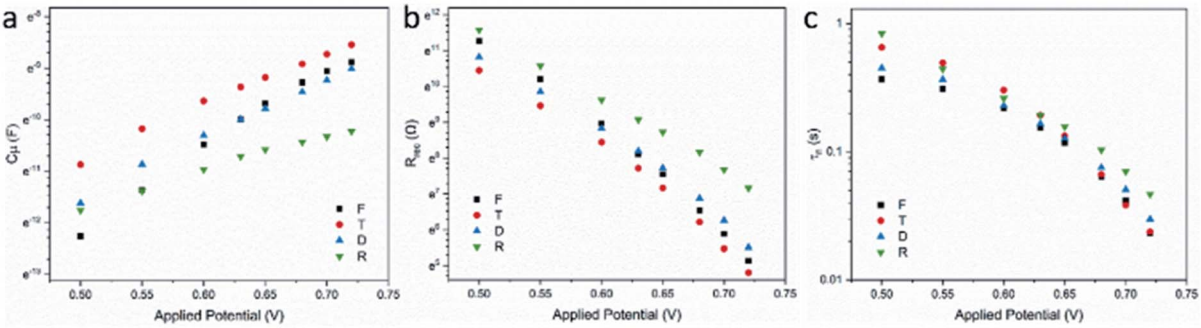

Fig. 8 (a) Chemical capacitance C_μ, (b) recombination resistance R_{rec} and (c) electron lifetime τ_n of single-layer photoanodes as a function of applied bias potential under white light LED illumination.

each TiO_2 was also obtained and shown in Table S3.† The highest β for cell F implies its stronger potential dependence of R_{rec}. It has been reported that the β value tells the degree of the impact from surface states on the charge recombination.[56] If $\beta = 1$, the charge recombination solely happens from the conduction band of TiO_2. When β is less than 1, which is normally observed in DSSCs, lower β indicates more contribution from the surfaces states to the charge recombination. Based on this, a more ideal charge recombination occurs in cell F (higher β), which is likely because of its shallower distribution of trap states as discussed above.

In order to determine the effect of recombination kinetics on the cell performance, it is also useful to plot R_{rec} *versus* total electron density (n), which can be obtained from C_μ by the following equation[57]

$$n = \frac{k_B T}{\alpha q^2 L} C_\mu \quad (5)$$

As shown in Fig. S8,† cell F shows slightly lower R_{rec} at a fixed n compared with cell D, suggesting slightly faster recombination at the surface of $mcTiO_2$ in cell F. Also taking D as the reference, R showed similar kinetics and T showed the slowest. By comparing R_{rec} *versus* potential and R_{rec} *versus* n plots, one can observe an obvious shift of R and T, which means recombination kinetics is not the determinant of R_{rec} at fixed potential. One possible reason is that their different crystallinity and surface states (denoted by N_s) make more contributions to the value of R_0 therefore R_{rec}. The smallest N_s for sample R leads to the highest R_{rec} among all TiO_2, while the highest N_s for sample T due to the highest surface area drops off its R_{rec} in potential plots. This is also consistent with the conclusion based on the C_μ analysis. For cell F, considering the similar surface states between cell F and cell D, the slightly faster recombination kinetics results in slightly lower R_{rec} at high applied potential. However, at lower applied potential, R_{rec} of cell F becomes higher compared with cell D, which can be attributed to its shallower trap distribution. From eqn (2), the position of conduction band of TiO_2 also alters the value of R_0 therefore R_{rec} when different TiO_2 is applied as photoanodes. Even though CB edge shifts of TiO_2 with exposed {001} facets have been detected and reported in some published reports,[58] the impact of this on R_{rec} is not significant here by comparing cell F and cell D. Electron lifetime calculated from $\tau_n = R_{rec} \times C_\mu$ was also plotted *versus* applied potential (Fig. 8c) and total electron concentration (Fig. S8†). The lifetime follows the same trends as R_{rec} in both plots, further supporting the discussion based on R_{rec} results.

On the basis of the above characterization and analysis, it can be seen that $mcTiO_2$ possesses similar dye uptake capability to commercial nanoparticle TiO_2 due to the high surface area from nanosized building-blocks, excellent light scattering behaviour similar to commercial large-size particles because of the overall mesocrystal size, and reasonable electron transport ability and recombination resistance, resulting from the porous mesocrystal structure and the crystallographic order of nanoparticles. Such a combination of properties in one material makes TiO_2 mesocrystals promising photoanodes for DSSCs and also prospective candidates in other applications. However, the high reflectance may limit its performance in single-layer photoelectrodes. To make the best use of all the properties from the specific structure, $mcTiO_2$ was also tested as

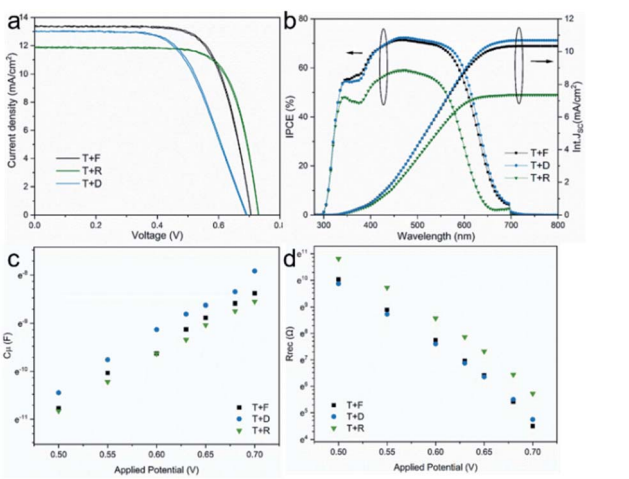

Fig. 9 (a) J–V curves and (b) IPCE spectrum of DSSCs using $mcTiO_2$ and reference TiO_2 as scattering layer, (c) chemical capacitance and (d) recombination resistance as a function of applied bias potential under white light LED illumination.

Table 2 Comparison of dye uptake capabilities and photovoltaic properties for different TiO_2 as scattering layer

TiO_2	Dye loading (nmol cm^{-2})	V_{OC} (V)	J_{SC} (mA cm^{-2})	FF	PCE (%)
T + F	108.78	0.71 (0.70 ± 0.01)	13.42 (13.1 ± 0.18)	0.71 (0.67 ± 0.04)	6.73 (6.10 ± 0.47)
T + D	105.03	0.69 (0.69 ± 0.01)	13.04 (13.0 ± 0.12)	0.61 (0.59 ± 0.01)	5.53 (5.28 ± 0.15)
T + R	71.36	0.73 (0.72 ± 0.01)	11.89 (11.9 ± 0.07)	0.74 (0.69 ± 0.03)	6.43 (5.91 ± 0.33)

[a] Mean values ± s.d. are shown, as obtained from 3 devices for T + R, and 5 devices for T + F.

a scattering layer on top of transparent nanoparticle TiO_2 films made from Solaronix T. In this configuration, as shown in the schematic illustration (Fig. S9†), the portion of light which passes through the transparent layer will be scattered for greater path length following Mie's scattering theory.[39] As a result, optimal light harvesting can be reached when both layers possess excellent dye coverage. Compared with commercial reflective $TiO_{2\ in\ T+R}$, $mcTiO_2$ in T + F has similar light scattering (see Fig. S9†) but higher dye loading in the scattering layer, leading to better utilization of forward scattered light therefore higher J_{SC} as shown in Fig. 9a and Table 2. Compared with commercial diffuse TiO_2 in T + D, $mcTiO_2$ in T + F has higher light reflection. But the presence of the transparent layer avoids waste of the backward scattered light. As a consequence of the optimised light harvesting, T + F showed similar current to T + D. This was consistent with the recorded incident photon-to-current conversion efficiency (IPCE) spectra and integrated J_{SC} from IPCE spectra (Fig. 9b), showing similar IPCE from T + F and T + D and lower maximum with T + R.

The average V_{OC} of DSSCs is 0.70 ± 0.01 V, 0.69 ± 0.01 V, and 0.72 ± 0.01 V for T + F, T + D and T + R, respectively. This is consistent with their inverse order of chemical capacitance and the order of recombination resistance, as shown in Fig. 9c and d. Exponential trap distribution parameter α for three two-layers photoanodes was also calculated based on Fig. 9c and listed in Table S4.† It is not surprising that they have similar α values, therefore similar trap distribution, since commercial nanoparticle TiO_2 (T) was used as main working layer in all three photoanodes. The additional scattering layer modifies the electronic structure of the three photoanodes to varying degrees. In terms of C_μ, three photoelectrodes follow the order T + D > T + F > T + R. As discussed above, the lowest C_μ of T + R may come from the lowest total number of trap states, which is because of the high crystallinity of R. For T + F and T + D, considering their similar α and close crystallinity of $mcTiO_2$ and diffractive TiO_2 (D), the lower C_μ of T + F can be ascribed to the positive shift of CB edge according to eqn (2). This interpretation can be corroborated by R_{rec} analysis. From Fig. S10,† T + F has the lowest R_{rec} at fixed total electron concentration, indicating the recombination is faster on the surface of T + F, consistent with the observations in single-layer DSSCs. T + D and T + R have similar recombination kinetics. The smallest surface area of R leads to the lowest N_s therefore the highest R_{rec} at fixed potential, in line with the highest V_{OC} of T + R. The N_s of T + F and T + D are regarded to be similar because of their similar surface area estimated from dye uptake and similar trap distribution depth from the same α value. In this case, there should be some impacts from other aspects to offset the fast recombination kinetics of T + F in order to endow it with comparable R_{rec} at fixed applied potential and slightly higher V_{OC} under 1 sun illumination compared with T + D. According to eqn (4), the aforementioned positive CB edge shift of $mcTiO_2$ in T + F may explain the results.

The long-term stability of DSSCs using different TiO_2 as scattering layers was evaluated by recording the PCE of cells kept in dark and ambient condition. The results are given in Fig. S11.† After 92 days, the cell T + F still showed 96.8% of the initial efficiency, as good as the cells based on all commercial TiO_2 photoanodes.

Conclusions

In summary, we have demonstrated a facile and versatile method to prepare mesocrystal films by making the printable paste of the topotactic precursor followed by *in situ* topotactic transformation of printed films. In this work we prove that this technique works very well for anatase TiO_2. The obtained $mcTiO_2$ from printed NH_4TiOF_3 films possesses typical structural features of mesocrystals, which brings properties associated with individual nanoparticles, advantages from the crystallographic orientation of nanoparticles and collective functions of the mesocrystal. In a specific application, DSSCs, we applied the $mcTiO_2$ as single-layer photoanodes, in which the properties from the structural features were discussed and compared with commercial TiO_2 in detail; and also as scattering layer to make better use of all the structural properties. Compared with commercial scattering TiO_2, $mcTiO_2$ showed a better performance as the scattering layer owing to its high dye loading capacity, superior visible light scattering and reasonable charge transport. We believe that the $mcTiO_2$ films from *in situ* topotactic transformation could also make the best use of the structural features in other applications using porous TiO_2. Furthermore, this method simplifies manufacturing processes for mesocrystal films and opens up general opportunities for other functional ceramic films.

Author contributions

BL designed, carried out and analysed most of the practical work and drafted the manuscript. AVO carried out confirmatory PCE measurements and the IPCE measurements. NR directly supervised most of the work and both NR and AI inputted into manuscript preparation and results interpretation.

Conflicts of interest

There are no conflicts to declare.

Acknowledgements

The authors thank Dr Aaron Naden for TEM measurements in the University of St. Andrews. We thank Dr Nicola Cayzer for help with the SEM images acquisition. B. L. gratefully acknowledges China Scholarship Council and The University of Edinburgh for a PhD scholarship. A. I. acknowledges UK Research and Innovation (UKRI), Engineering and Physical Sciences Research Council (EPSRC) for the Fellowship grant (EP/P011500/1), the EPSRC ECR Capital Equipment grant and ScotCHEM for funding IPCE setup.

References

1 S. Franz, H. Arab, G. L. Chiarello, M. Bestetti and E. Selli, *Adv. Energy Mater.*, 2020, **10**, 2000652.
2 H. Wei, E. F. Rodriguez, A. F. Hollenkamp, A. I. Bhatt, D. Chen and R. A. Caruso, *Adv. Funct. Mater.*, 2017, **27**, 1703270.
3 S. So, I. Hwang, J. Yoo, S. Mohajernia, M. Mačković, E. Spiecker, G. Cha, A. Mazare and P. Schmuki, *Adv. Energy Mater.*, 2018, **8**, 1800981.
4 Z. Zheng, F. Zhuge, Y. Wang, J. Zhang, L. Gan, X. Zhou, H. Li and T. Zhai, *Adv. Funct. Mater.*, 2017, **27**, 1703115.
5 A. H. Mamaghani, F. Haghighat and C. S. Lee, *J. Photochem. Photobiol. Chem.*, 2019, **378**, 156–170.
6 B. O'Regan and M. Grätzel, *Nature*, 1991, **353**, 737–740.
7 E. J. W. Crossland, N. Noel, V. Sivaram, T. Leijtens, J. A. Alexander-Webber and H. J. Snaith, *Nature*, 2013, **495**, 215–219.
8 N. Vlachopoulos, A. Hagfeldt, I. Benesperi, M. Freitag, G. Hashmi, G. Jia, R. A. Wahyuono, J. Plentz and B. Dietzek, *Sustain. Energy Fuels*, 2021, **5**, 367–383.
9 M. Kokkonen, P. Talebi, J. Zhou, S. Asgari, S. A. Soomro, F. Elsehrawy, J. Halme, S. Ahmad, A. Hagfeldt and S. G. Hashmi, *J. Mater. Chem. A*, 2021, **9**, 10527–10545.
10 J. Maçaira, L. Andrade and A. Mendes, *Sol. Energy Mater. Sol. Cells*, 2016, **157**, 134–138.
11 S. Ashraf, R. Su, J. Akhtar, H. M. Siddiqi, A. Shuja and A. El-Shafei, *Sol. Energy*, 2020, **199**, 74–81.
12 Q. Huaulmé, V. M. Mwalukuku, D. Joly, J. Liotier, Y. Kervella, P. Maldivi, S. Narbey, F. Oswald, A. J. Riquelme, J. A. Anta and R. Demadrille, *Nat. Energy*, 2020, **56**(5), 468–477.
13 Z.-Q. Li, Y.-P. Que, L.-E. Mo, W.-C. Chen, Y. Ding, Y.-M. Ma, L. Jiang, L.-H. Hu and S.-Y. Dai, *ACS Appl. Mater. Interfaces*, 2015, **7**, 10928–10934.
14 F. Zhao, R. Ma and Y. Jiang, *Appl. Surf. Sci.*, 2018, **434**, 11–15.
15 N. Fu, Y. Liu, Y. Liu, W. Lu, L. Zhou, F. Peng and H. Huang, *J. Mater. Chem. A*, 2015, **3**, 20366–20374.
16 Z.-Q. Li, L.-E. Mo, W.-C. Chen, X.-Q. Shi, N. Wang, L.-H. Hu, T. Hayat, A. Alsaedi and S.-Y. Dai, *ACS Appl. Mater. Interfaces*, 2017, **9**, 32026–32033.
17 X. Miao, K. Pan, Y. Liao, W. Zhou, Q. Pan, G. Tian and G. Wang, *J. Mater. Chem. A*, 2013, **1**, 9853–9861.
18 H. Cölfen and M. Antonietti, *Angew. Chem., Int. Ed.*, 2005, **44**, 5576–5591.
19 J. Seto, Y. Ma, S. A. Davis, F. Meldrum, A. Gourrier, Y.-Y. Kim, U. Schilde, M. Sztucki, M. Burghammer, S. Maltsev, C. Jäger and H. Cölfen, *Proc. Natl. Acad. Sci. U.S.A.*, 2012, **109**, 3699–3704.
20 A.-W. Xu, M. Antonietti, H. Cölfen and Y.-P. Fang, *Adv. Funct. Mater.*, 2006, **16**, 903–908.
21 D. Wu, Y. Wang, N. Ma, K. Cao, W. Zhang, J. Chen, D. Wang, Z. Gao, F. Xu and K. Jiang, *Electrochim. Acta*, 2019, **305**, 474–483.
22 L. Zhou, D. Smyth-Boyle and P. O'Brien, *J. Am. Chem. Soc.*, 2008, **130**, 1309–1320.
23 Z. Zhang, H. Nagashima and T. Tachikawa, *Angew. Chem.*, 2020, **132**, 9132–9139.
24 W. Cao, W. Wang, H. Shi, J. Wang, M. Cao, Y. Liang and M. Zhu, *Nano Res.*, 2018, **11**, 1437–1446.
25 G. Zhu, J. Yang, C. Bao, X. Zhang, Z. Ji, S. Wu and X. Shen, *J. Colloid Interface Sci.*, 2016, **468**, 136–144.
26 D. Wu, K. Cao, H. Wang, F. Wang, Z. Gao, F. Xu, Y. Guo and K. Jiang, *J. Colloid Interface Sci.*, 2015, **456**, 125–131.
27 M. Di, Y. Li, H. Wang, Y. Rui, W. Jia and Q. Zhang, *Electrochim. Acta*, 2018, **261**, 365–374.
28 Y. Guo, H. Li, J. Chen, X. Wu and L. Zhou, *J. Mater. Chem. A*, 2014, **2**, 19589–19593.
29 H. You, Q. Wu, J. Li, S. He, X. Li, X. Yang, J. Yang, Y. Meng, S. Tong and M. Wu, *CrystEngComm*, 2017, **19**, 2456–2463.
30 J. Ye, W. Liu, J. Cai, S. Chen, X. Zhao, H. Zhou and L. Qi, *J. Am. Chem. Soc.*, 2011, **133**, 933–940.
31 P. Liu, K. Zhu, K. Bian, Y. Xu, F. Zhang, W. Zhang, W. Huang and J. Zhang, *J. Power Sources*, 2018, **395**, 158–162.
32 L. Zhou, D. S. Boyle and P. O'Brien, *Chem. Commun.*, 2007, 144–146.
33 T. Shinagawa, M. Watanabe, J. Tani and M. Chigane, *Cryst. Growth Des.*, 2017, **17**, 3826–3833.
34 X. Y. Kong, T. Tong, B.-J. Ng, J. Low, T. H. Zeng, A. R. Mohamed, J. Yu and S.-P. Chai, *ACS Appl. Mater. Interfaces*, 2020, **12**, 26991–27000.
35 F. Xie, G. Dong, K. Wu, Y. Li, M. Wei and S. Du, *Chem. Phys. Lett.*, 2020, **739**, 136996.
36 S. Ito, T. N. Murakami, P. Comte, P. Liska, C. Grätzel, M. K. Nazeeruddin and M. Grätzel, *Thin Solid Films*, 2008, **516**, 4613–4619.
37 O. Boytsova, I. Dovgaliuk, D. Chernyshov, A. Eliseev, P. O'Brien, A. J. Sutherland and A. Bosak, *J. Appl. Crystallogr.*, 2019, **52**, 23–26.
38 C. F. Macrae, I. Sovago, S. J. Cottrell, P. T. A. Galek, P. McCabe, E. Pidcock, M. Platings, G. P. Shields, J. S. Stevens, M. Towler and P. A. Wood, *J. Appl. Crystallogr.*, 2020, **53**, 226–235.
39 G. Mie, *Ann. Phys.*, 1908, **330**, 377–445.
40 E. Hao, N. A. Anderson, J. B. Asbury and T. Lian, *J. Phys. Chem. B*, 2002, **106**, 10191–10198.
41 Y. J. Son, J. S. Kang, J. Yoon, J. Kim, J. Jeong, J. Kang, M. J. Lee, H. S. Park and Y. E. Sung, *J. Phys. Chem. C*, 2018, **122**, 7051–7060.

42 J. Zhu, S. Wang, Z. Bian, S. Xie, C. Cai, J. Wang, H. Yang and H. Li, *CrystEngComm*, 2010, **12**, 2219–2224.
43 Y. Liu, Y. Zhang and J. Wang, *CrystEngComm*, 2012, **15**, 791–801.
44 N. M. Laptash, I. G. Maslennikova and T. A. Kaidalova, *J. Fluorine Chem.*, 1999, **99**, 133–137.
45 R. Karthik, N. Karikalan and S. M. Chen, *Carbohydr. Polym.*, 2017, **164**, 102–108.
46 C. Yao, X. Yin, Y. Yu, Z. Cai and X. Wang, *Adv. Funct. Mater.*, 2017, **27**, 1700794.
47 E. Gabrielsson, H. Ellis, S. Feldt, H. Tian, G. Boschloo, A. Hagfeldt, L. Sun, E. Gabrielsson, H. Tian, L. Sun, H. Ellis, S. M. Feldt, G. Boschloo and A. Hagfeldt, *Adv. Energy Mater.*, 2013, **3**, 1647–1656.
48 F. Fabregat-Santiago, J. Bisquert, G. Garcia-Belmonte, G. Boschloo and A. Hagfeldt, *Sol. Energy Mater. Sol. Cells*, 2005, **87**, 117–131.
49 S. R. Raga, E. M. Barea and F. Fabregat-Santiago, *J. Phys. Chem. Lett.*, 2012, **3**, 1629–1634.
50 J. A. Anta, F. Casanueva and G. Oskam, *J. Phys. Chem. B*, 2006, **110**, 5372–5378.
51 F.-S. Francisco, I. Mora-Seró, A. Germà Garcia-Belmonte and J. Bisquert, *J. Phys. Chem. B*, 2002, **107**, 758–768.
52 W. Yan, M.-M. Huo, R. Hu and Y. Wang, *RSC Adv.*, 2019, **9**, 1734–1740.
53 T. Berger, T. Lana-Villarreal, D. Monllor-Satoca and R. Gómez, *J. Phys. Chem. C*, 2007, **111**, 9936–9942.
54 Z. M. Beiley, E. T. Hoke, R. Noriega, J. Dacuña, G. F. Burkhard, J. A. Bartelt, A. Salleo, M. F. Toney and M. D. McGehee, *Adv. Energy Mater.*, 2011, **1**, 954–962.
55 J. Lin, M. Guo, C. T. Yip, W. Lu, G. Zhang, X. Liu, L. Zhou, X. Chen and H. Huang, *Adv. Funct. Mater.*, 2013, **23**, 5952–5960.
56 Q. Wang, S. Ito, M. Grätzel, F. Fabregat-Santiago, I. Mora-Seró, J. Bisquert, B. Takeru and H. Imai, *J. Phys. Chem. B*, 2006, **110**, 25210–25221.
57 P. R. F. Barnes, K. Miettunen, X. Li, A. Y. Anderson, T. Bessho, M. Gratzel and B. C. O'Regan, *Adv. Mater.*, 2013, **25**, 1881–1922.
58 J. De Peng, H. H. Lin, C. T. Lee, C. M. Tseng, V. Suryanarayanan, R. Vittal and K. C. Ho, *RSC Adv.*, 2016, **6**, 14178–14191.